Chinese Chemical Letters 36 (2025) 109555

Contents lists available at ScienceDirect

Chinese Chemical Letters

journal homepage: www.elsevier.com/locate/cclet

Support effect and confinement effect of porous carbon loaded tin dioxide nanoparticles in high-performance CO_2 electroreduction towards formate

Xingxing Jiang[1], Yuxin Zhao[1], Yan Kong, Jianju Sun, Shangzhao Feng, Xin Lu, Qi Hu, Hengpan Yang*, Chuanxin He*

College of Chemistry and Environmental Engineering, Shenzhen University, Shenzhen 518060, China

ARTICLE INFO

Article history:
Received 12 December 2023
Revised 10 January 2024
Accepted 19 January 2024
Available online 24 January 2024

Keywords:
CO_2 electroreduction
Support effect
Porous carbon fiber
Formate
Mass activity

ABSTRACT

Leveraging the interplay between the metal component and the supporting material represents a cornerstone strategy for augmenting electrocatalytic efficiency, *e.g.*, electrocatalytic CO_2 reduction reaction (CO_2RR). Herein, we employ freestanding porous carbon fibers (PCNF) as an efficacious and stable support for the uniformly distributed SnO_2 nanoparticles (SnO_2PCNF), thereby capitalizing on the synergistic support effect that arises from their strong interaction. On one hand, the interaction between the SnO_2 nanoparticles and the carbon support optimizes the electronic configuration of the active centers. This interaction leads to a noteworthy shift of the d-band center toward stronger intermediate adsorption energy, consequently lowering the energy barrier associated with CO_2 reduction. As a result, the SnO_2PCNF realizes a remarkable CO_2RR performance with excellent selectivity towards formate (98.1%). On the other hand, the porous carbon fibers enable the uniform and stable dispersion of SnO_2 nanoparticles, and this superior porous structure of carbon supports can also facilitate the exposure of the SnO_2 nanoparticles on the reaction interface to a great extent. Consequently, adequate contact between active sites, reactants, and electrolytes can significantly increase the metal utilization, eventually bringing forth a remarkable 7.09 A/mg mass activity. This work might provide a useful idea for improving the utilization rate of metals in numerous electrocatalytic reactions.

© 2024 Published by Elsevier B.V. on behalf of Chinese Chemical Society and Institute of Materia Medica, Chinese Academy of Medical Sciences.

Increasing concentration of atmospheric CO_2 is a worldwide concern and continues to trigger various environmental problems [1,2]. Electrocatalytic CO_2 reduction reaction utilizing intermittent renewable electricity, driven by wind and solar, presents a promising avenue to facilitate the carbon cycle due to its sustainable nature and the valuable products yielded in this procedure [3–5]. CO_2 can be converted into a variety of reduction products such as carbon monoxide, formic acid, methanol, methane, ethanol, and ethylene [6]. Among the above carbonaceous compounds, formate (formic acid) is regarded as one of the ideal value-added products with low toxicity and flammability. Formate has a wide range of applications in the chemical industry and can also be used for direct formic acid fuel cells (DFAFC) [7]. However, the dynamic process of CO_2RR is typically slow and inefficient due to the electrochemical inert of CO_2 molecules and the competing hydrogen evolution reaction (HER) [8–10]. As a result, the development of highly efficient and selective catalysts for CO_2RR to formate has emerged as a research priority.

At present, the metal-based catalysts (such as Sn and Bi) have been regarded as the most promising alternatives for CO_2RR to formate [11–13]. Some efforts have been reported to overcome the sluggish kinetics and enhance the efficiency for formate production, including tuning the size, shape, composition, and crystallinity of the metallic component [14–18]. Besides, the dispersion of active metal nanoparticles (NPs) on supports is also an effective strategy to improve the utilization rate of metals and thus reduce catalyst costs [19–21]. Additionally, upon interaction with the support material, the metal active centers demonstrate heightened metal-support interactions attributed to the increased prevalence of interface sites. These interactions not only bolster stability but also exert a profound influence on the electronic configuration of the metal, subsequently exerting a pivotal role in shaping its catalytic characteristics [22,23]. For example, Xu and coworkers reported an electronic metal–support interaction between Cu and *a*-C on Cu-based MOF, achieving high selective and stable CO_2

---

* Corresponding authors.
E-mail addresses: hpyang@szu.edu.cn (H. Yang), hecx@szu.edu.cn (C. He).

[1] These authors contributed equally to this work.

https://doi.org/10.1016/j.cclet.2024.109555
1001-8417/© 2024 Published by Elsevier B.V. on behalf of Chinese Chemical Society and Institute of Materia Medica, Chinese Academy of Medical Sciences.

electroreduction to CH_4 [24]. Other reports also showed that the incorporation of various supports, such as carbon-based materials or metal compounds (including metal oxides and metal carbides), in conjunction with metal active centers, can manifest significantly enhanced electrocatalytic activity, compared to catalysts lacking such support [20,25-27]. Among these varieties of loading support, porous carbon fibers (PCF), which amalgamate the structural and functional attributes of conventional carbon fibers and porous carbon materials, have garnered significant attention in a broad spectrum of applications including energy conversion and storage, catalysis, adsorption and separation, sensing, and various other domains [28–31]. Compared with traditional porous carbon powder materials that require an insulating binder, PCF stands out as an exemplary binder-free, self-supporting, robust material characterized by its fibrous morphology and well-defined porous architecture. Therefore, the architectures, morphological characteristics, and elemental compositions of PCFs, along with the integration of active materials, are regarded as pivotal factors for enhancing their efficacy in the realms of energy and environmental applications [32,33].

In this work, we designed a SnO_2 nanoparticles loading free-standing porous carbon nanofibers (SnO_2PCNF) catalyst *via* simple electrospinning technology and later hydrothermal method. As a potential loading support, porous carbon fiber gives full play to its porous local confinement effect to the dispersed SnO_2 particles. DFT calculations showed that after interaction between SnO_2 particles and carbon nanofibers, the oxidation state of Sn was enhanced to a higher $Sn^{\delta+}$ peak and the d-band center of active sites Sn was shifted to be more conducive for the CO_2 to formate process. Compared with the bulk SnO_2, SnO_2 loaded general carbon fiber (SnO_2CNF), the discernible impact of the porous structure and support effects on SnO_2PCNF can be unequivocally attributed to the substantial enhancement of current density, Faraday efficiency, and mass activity in the electrocatalytic reduction of CO_2 to formate.

The dispersed SnO_2 nanoparticles loaded on porous carbon nanofibers (denoted as SnO_2PCNF) were synthesized *via* electrospinning and pyrolysis followed by the hydrothermal method, as shown schematically in Fig. 1a. First, the zeolitic imidazolate framework-8 (ZIF-8) were fabricated as pore former *via* a facile liquid-solid-solution method and homogeneously dispersed in PAN solution for electrospinning to obtain nanofibers precursors. Subsequently, porous carbon nanofibers were fabricated as a stable substrate with the evaporation of the Zn precursor *via* pyrolysis in the argon atmosphere. Finally, SnO_2 nanoparticles were grown *in situ* on porous carbon nanofibers by hydrothermal method. For comparison, the SnO_2 nanoparticles, bare porous carbon fibers (PCNF) and SnO_2 nanoparticles loaded on carbon nanofibers (SnO_2CNF) were also synthesized to research the effects on carbon supports and SnO_2 nanoparticles. The details were shown in Supporting information.

The morphology evolutions from PCNF to SnO_2, SnO_2CNF, and SnO_2PCNF were characterized using multiple methods. The as-obtained SnO_2PCNF catalyst is a flexible and self-supporting carbon membrane, which can be prepared at least 240 square centimeters in one single time under existing implementation conditions (Fig. 1b). As displayed in Fig. S1 (Supporting information), the scanning electron microscope (SEM) images show that the one-dimensional nanofibers framework in PCNF, SnO_2CNF and SnO_2PCNF are all well preserved after pyrolysis and the later hydrothermal treatments. Notably, in Fig. S1c, the size of the SnO_2 nanoparticles is hard to determine since they are agglomerated. The transmission electron microscopy (TEM) image in Fig. S2 (Supporting information) further demonstrates that the PCNF has an interconnected porous skeleton, which could provide abundant

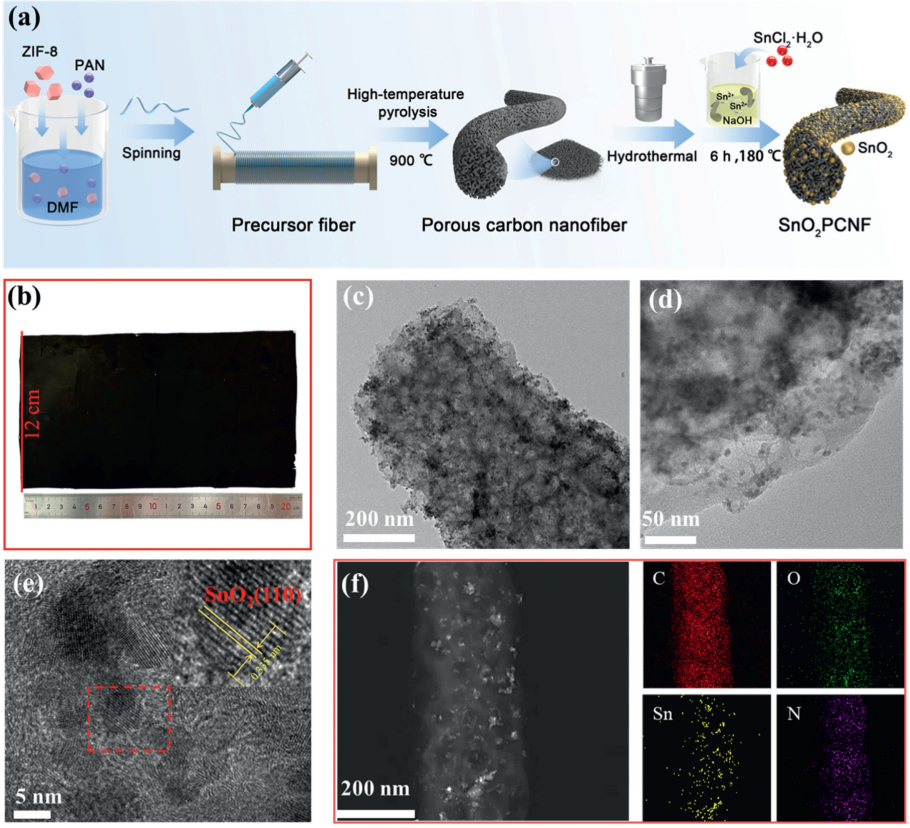

Fig. 1. (a) Synthesis scheme of the SnO_2PCNF. (b) The free-standing fiber membrane of SnO_2PCNF. (c) TEM image of SnO_2PCNF. (d, e) HR-TEM images of SnO_2PCNF. (f) HAADF-STEM-EDS elemental mapping images for SnO_2PCNF.

channels for SnO_2 nanoparticle loading. In addition, Fig. 1c shows that the SnO_2 loaded on PCNF can be effectively dispersed, and the high-resolution TEM (HR-TEM) in Fig. 1d and Fig. S3 (Supporting information) indicate an average particle size of about 5 nm. Moreover, Fig. 1e exhibits a set of lattice fringe on SnO_2PCNF with an interplanar distance of 0.335 nm, indexed to the (110) plane of SnO_2. The elemental mapping images of SnO_2PCNF in Fig. 1f show that C, O, Sn, and N elements are homogeneously distributed in the PCNF support. As a comparison, TEM images in Fig. S4 (Supporting information) of SnO_2 and SnO_2CNF are also investigated, which further proves the importance of ZIF-8 as a pore former for SnO_2 nanoparticle loading.

X-ray powder diffraction (XRD) was further employed to obtain the crystal structure information of these synthesized samples. In Fig. 2a, unlike the bare PCNF, all peaks of the SnO_2-contained samples are well-matched with the rutile-type tetragonal SnO_2 (PDF #88-0287). To gain more insight into the porous structure of PCNF, SnO_2CNF and SnO_2PCNF, N_2 adsorption–desorption analysis and pore size distribution were characterized (Fig. 2b and Fig. S5 in Supporting information). It is evident that PCNF exhibits the highest specific surface area, measuring at 184.16 m^2/g, and encompasses a broad spectrum of pore sizes, manifesting a layered porous structure consisting of both micropores and mesoporous pores. As a comparison, the BET surface areas of SnO_2, SnO_2CNF and SnO_2PCNF are listed in Table S1 (Supporting information). When juxtaposed with the CO_2 adsorption curve depicted in Fig. 2c, it becomes apparent that the porous structure in the catalyst facilitates the dispersion and growth of SnO_2 nanoparticles, along with the efficient penetration of the electrolyte and rapid ion diffusion during the CO_2RR process. It is indicated that a subsequent hydrothermal reaction loading SnO_2 nanoparticles appears to reduce the specific surface area of the porous carbon fibers, but also optimizes the pore size distribution on the carbon fibers. Meanwhile, the FT-IR spectra of PCNF, SnO_2, SnO_2CNF and SnO_2PCNF were recorded at transmittance mode (Fig. 2d). The peak at 607 cm^{-1} on SnO_2 is attributed to the Sn–O stretching [34]. From this spectrum, the peaks of Sn-O stretching on SnO_2CNF and SnO_2PCNF are clearly redshifted compared to the SnO_2 sample, which represents electron migration and the lattice constant decreases.

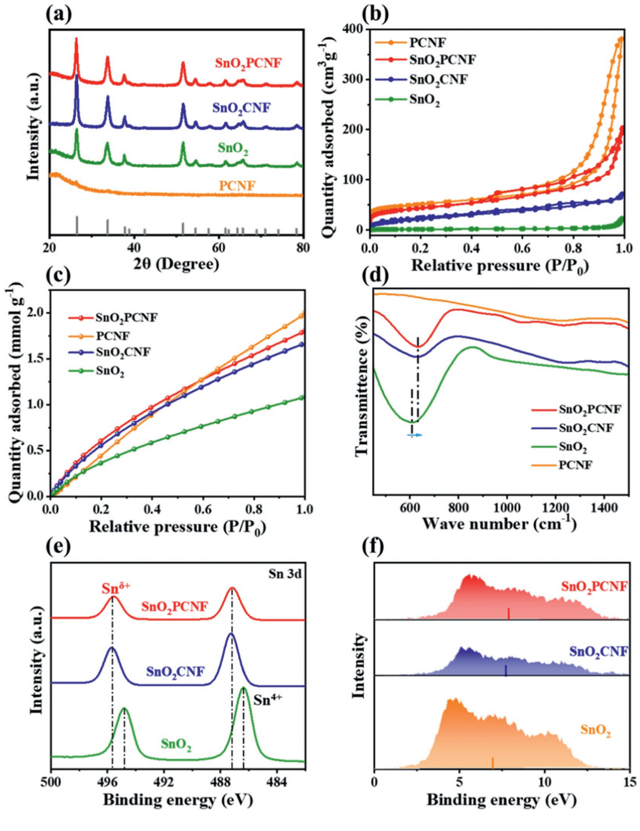

Fig. 2. (a) XRD patterns, (b) N_2 adsorption/desorption isotherms, (c) CO_2 adsorption isotherms, (d) FT-IR spectra of PCNF, SnO_2, SnO_2CNF and SnO_2PCNF. (e) Sn 3d XPS spectra, (f) valence band spectra of SnO_2, SnO_2CNF and SnO_2PCNF.

Furthermore, the chemical compositions of these four samples were characterized by X-ray photoelectron spectra (XPS). The signals of C, O, Sn, and N elements are identified in the survey spectrum. As a comparison of Sn 3d XPS spectra in Fig. 2e, the signal peaks at 487.1 eV/595.6 eV are much higher than the Sn^{4+} peak (486.3 eV/594.8 eV) on SnO_2, which represents an enhanced of the Sn oxidation (denoted as $Sn^{\delta+}$). In Figs. S6 and S7 (Supporting information), the C 1s, and N 1s XPS spectra of these four samples, combined with the Raman spectra (Fig. S8 in Supporting information), demonstrate a stable nitrogen-containing carbon substrate and stronger binding energy of Sn=O bonds from electronic structure optimization [15,35]. Therefore, further characterization was carried out with the surface valence band photoemission spectra to explore the d-band center of SnO_2, SnO_2CNF and SnO_2PCNF, which relates to the adsorption energy of an adsorbed molecule on transition metal sites [36,37]. In Fig. 2f, compared to SnO_2 (6.84 eV), the d-band center of SnO_2CNF (7.74 eV) and SnO_2PCNF (7.88 eV) upshifts. The changes in the d-band center have been proven to reduce the adsorption of C intermediates and enhance the adsorption of oxygen-containing intermediates during the CO_2RR process. These characteristics jointly reflect the support effects between SnO_2 and carbon substrates, which is embodied in the change of electronic structure.

To explore the CO_2RR performance, the catalytic performance of SnO_2/PCNF electrocatalysts for CO_2RR was evaluated in a gastight two-compartment H-cell with CO_2-saturated 0.1 mol/L $KHCO_3$ as the electrolyte. The free-standing SnO_2PCNF membrane can be tailored for testing in Fig. S9 (Supporting information). Compared with linear sweep voltammetry (LSV) curves in the N_2-saturated electrolyte, the current densities measured for these four catalysts in the CO_2-saturated catholyte show a dramatic increase, indicating that CO_2 is more favorably reduced with their intrinsic activity than the HER in the CO_2-saturated catholyte (Fig. S10 in Supporting information). The PCNF has the highest current density, which is greater than that of SnO_2PCNF, SnO_2CNF, and SnO_2 in turn (Fig. 3a). These current densities seem to be related to the specific surface area of the catalysts. Therefore, analysis of catalyst reduction products is needed to further evaluate the electrochemical properties of these catalysts. Specifically, the resultant products under different potentials were quantitatively analyzed with potentiostatic methods *via* online gas chromatography (GC) for gas products and ^{1}H nuclear magnetic resonance (^{1}H NMR) spectroscopy for liquid products (Figs. S11 and S12 in Supporting information). As shown in Fig. 3b, the FE of SnO_2PCNF for formate is higher than 70% over the wide potential ranges and it reached up to 86% at $-1.25\ V_{RHE}$ in the H-type cell, with effective suppression of the hydrogen evolution reaction and CO production. In Figs. S13a-c (Supporting information), SnO_2 had a maximum formate FE of 73.6% at $-1.65\ V_{RHE}$, while SnO_2CNF displayed a maximum formate FE of 84.5% at $-1.45\ V_{RHE}$. Besides, the PCNF shows a competitive HER activity with a maximum H_2 FE of 72% at $-1.45\ V_{RHE}$. As a comparison in Figs. 3c and d and Fig. S13d (Supporting information), the SnO_2PCNF exhibits the highest partial current density for formate of 24.8 mA/cm^2. According to current densities and Faradaic efficiency for the formate, SnO_2PCNF exhibits the best CO_2RR performance. Among them, SnO_2 as the active site provides excellent formate production, the interaction with carbon support improves

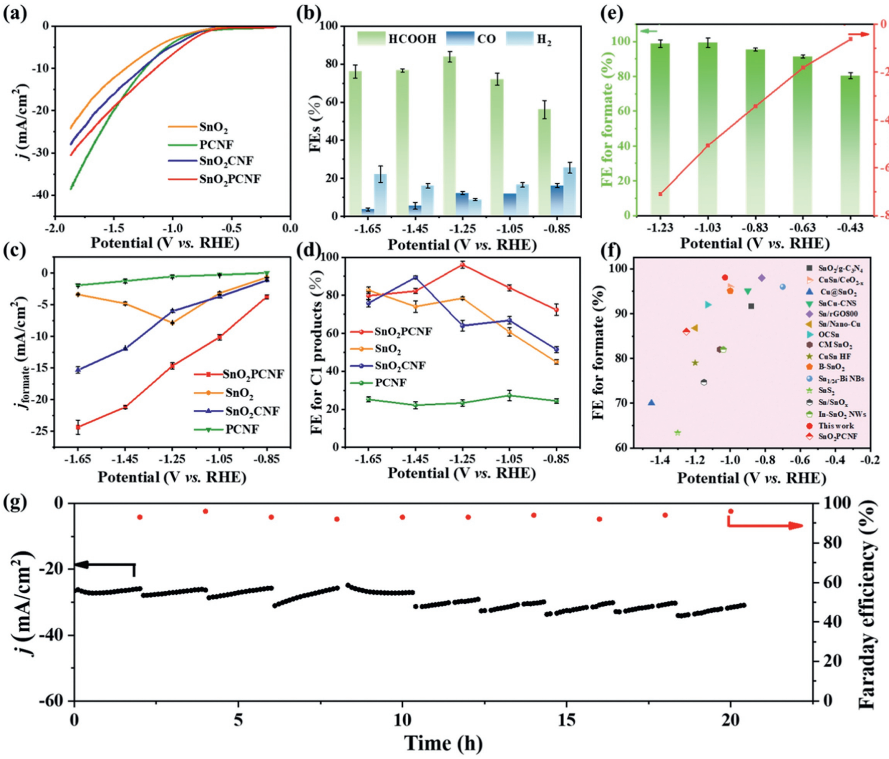

Fig. 3. (a) Comparisons of LSV curves of PCNF, SnO_2, SnO_2CNF and SnO_2PCNF in CO_2-saturated 0.1 mol/L $KHCO_3$ aqueous. (b) FEs of CO_2RR products on SnO_2PCNF. Comparisons of (c) the partial current densities for formate and (d) C_1 products at different applied potentials on PCNF, SnO_2, SnO_2CNF and SnO_2PCNF. (e) FE and mass active current for formate on flow-cell. (f) CO_2RR to formate performance comparisons of SnO_2PCNF with other Sn-based catalysts. (g) Long-term durability of SnO_2PCNF at −0.85 V for 21 h.

higher formate selectivity, and the porous structure increases the current density and lowers the applied potential at the highest formate faradaic efficiency.

To evaluate the electrocatalytic CO_2 conversion performance of the as-prepared SnO_2PCNF materials at current densities close to industrial relevance, a gas diffusion electrode (GDE) flow cell was used with 1 mol/L KOH solution as the electrolyte. In the GDE cell configuration, a continuous supply of gaseous CO_2 feedstock is channelled through the porous carbon support, facilitating direct access to the catalyst surface. This strategic approach effectively bypasses the constraints imposed by gas solubility limitations within the aqueous electrolyte. Concurrently, on the opposing side of the porous electrode, the electrolyte is methodically circulated over the catalyst surface using a peristaltic pump. This controlled flow of electrolyte can help to mitigate the accumulation of formate species at the catalyst surface, and act as a pH buffer to curb undue fluctuations in the electrolyte's pH. This orchestrated design seeks to minimize mass transfer limitations and enhance the overall efficiency of the system. As shown in Fig. 3e and Fig. S14 (Supporting information), the FE of SnO_2PCNF for formate is higher than 80% over the wide potential ranges from $-0.43\,V_{RHE}$ to $-1.23\,V_{RHE}$ and it reached up to 98.1% at $-1.05\,V_{RHE}$ in the flow cell. Moreover, a formate partial current density of 133 mA/cm^2 is achieved for SnO_2PCNF at $-1.23\,V_{RHE}$. The porous carbon nanofibers provide high exposure conditions for SnO_2 nanoparticles dispersed, so the wt% of Sn on PCNF is calculated as low as 3.69%. In Fig. 3f, the mass activity can reach up to 7.09 A/mg at $-1.23\,V_{RHE}$ on SnO_2PCNF, which is 124 times higher than that of bare SnO_2 nanoparticles (0.057 A/mg). In comparison to other previously reported Sn-based catalysts (Fig. 3f and Table S2 in Supporting information), it is evident that the SnO_2PCNF demonstrates a competitive performance in the electrochemical reduction of CO_2 to formate.

To precisely ascertain the impact of both the inherent characteristics and quantity of active sites during the electrolysis process, we conducted an evaluation of the electrochemical surface area (ECSA) for the freshly prepared catalysts. This evaluation was performed by quantifying the double-layer capacitance (C_{dl}) in the non-Faradaic potential region within an H-type electrochemical cell (Figs. S15 and S16a in Supporting information). The ECSA of these catalysts is in accordance with the previously investigated surface area from the BET test. Since the catalytic activity of PCNF is mainly hydrogen evolution, the ECSA for SnO_2PCNF is the highest for CO_2RR which is 7 times and 20 times than that of SnO_2CNF and SnO_2, respectively. Electrochemical impedance spectroscopy (EIS) was carried out to gain further insight into CO_2RR kinetics. The Nyquist plots demonstrate that SnO_2PCNF shows much smaller interfacial charge-transfer resistance during the CO_2 reduction process (Fig. S16b in Supporting information), suggesting a favorable faradaic process. The long-term electrolysis tests at −0.85 V_{RHE} demonstrate the high stability of the SnO_2PCNF catalyst in CO_2RR procedure (Fig. 3g). Furthermore, the catalyst powder loaded on the electrode is easily detached in electrolyte using the traditional drop-coating method. SnO_2PCNF membrane owns good mechanical strength as well as the CO_2RR performance to formate. Meanwhile, the chemical composition and morphology of SnO_2PCNF were also undamaged after these long-time stability tests (Figs. S17 and S18 in Supporting information).

To monitor the reaction process and the intermediate species of CO_2RR on SnO_2PCNF, we carried out *in situ* electrochemical Raman spectroscopy tests. In Fig. 4a, the peaks at 410 cm^{-1} are ascribed to the Raman phonon modes of E_g and E_{2g} for the SnO_2 rutile phase structure [38]. Moreover, two obvious Raman peaks at 1068 cm^{-1} and 1015 cm^{-1} are ascribed to CO_3^{2-} and HCO_3^- respectively, which act as indicators to reflect the change in pH on the $KHCO_3$ electrolyte. Evidently, the peak intensities of CO_3^{2-} gradually

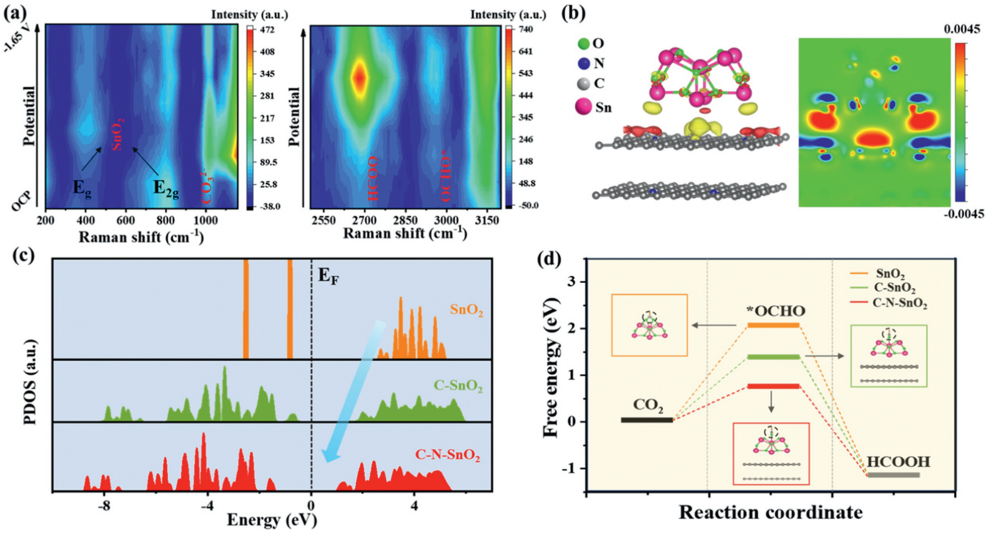

Fig. 4. (a) *In situ* Raman spectra collected of SnO_2PCNF at different applied potentials from OCP to −1.65 V_{RHE} in a 0.1 mol/L $KHCO_3$ electrolyte. (b) Charge density difference plots of SnO_2PCNF on the SnO_2-PCNF interface (The red and yellow areas represent charge consumption and accumulation). (c) PDOS of Sn 3d orbit and (d) reaction energy change of CO_2RR to formate on SnO_2, C-SnO_2 and C-N-SnO_2 models.

increase as the potential negatively shifts, representing a hydrogen proton consumption and the increase in pH value [39,40]. Besides, a stronger peak at 2713 cm^{-1} corresponding to $HCOO^-$ was observed, suggesting the promoted production of formate [41]. The intensifying peak located at 2966 cm^{-1} is attributed to the key intermediates OCHO* for the formate product during the electroreduction CO_2 process [42,43].

To gain deeper insights into the superiority of SnO_2PCNF in terms of support effect and formate production, density functional theory (DFT) calculations were implemented. Firstly, the charge density difference was used to analyze the electron interaction between the SnO_2 active sites and PCNF support. The theory SnO_2PCNF models (denoted as C-N-SnO_2 model) are presented as well as the comparable C-SnO_2 models in Figs. S19-S21 (Supporting information). After optimisation, the charge density difference plots are obtained (Fig. 4b, Figs. S22 and S23 Supporting information). The charge transfer mainly occurs from the Sn atom to the C/N substrate atoms and from the Sn/C atoms to the O atoms at the contact interface between SnO_2 and the C/N or C substrate. Moreover, the charge transfer is deeper in the SnO_2PCNF models, indicating a stronger interaction. The special charge transfer from Sn to C/N/O atoms in SnO_2PCNF is also in accordance with the discussion about the Sn oxidation modulation from the Sn 3d XPS spectra result. Secondly, to further understand the detailed contributions of the electronic structure, we further demonstrate the projected partial density of state (PDOS) in Fig. 4c. Eminently, compared to bulk SnO_2, the surface on C-SnO_2 and C-N-SnO_2 has displayed significantly downshifted 3d orbitals, suggesting the electronic structure modulations between the SnO_2 and the C or C/N substrate. The optimum electron transfer efficiency for the surface shows a higher electroactivity for CO_2RR. To understand the reaction process, the CO_2 reduction energy changes are compared to these three theory models. As previously detected by Raman spectroscopy, the intermediate *OCHO is the key to formate formation. The optimized *OCHO adsorption on the related theory models are shown in Figs. S24-S26 (Supporting information). The calculation for the free energy on CO_2RR process in Fig. 4d implies a lower energy barrier from CO_2 to the key intermediate *OCHO of 0.86 eV on C-N-SnO_2 than that of SnO_2 (2.1 eV) and C-SnO_2 (1.27 eV). This process also represents a rate-determining step for CO_2RR, thus indicating an excellent performance of SnO_2PCNF about higher formate selectivity and lower reaction applied potentials.

In conclusion, the SnO_2 nanoparticles have been successfully loaded on freestanding porous carbon fibers to achieve high performance of CO_2RR to formate with 98.1% selectivity. According to DFT calculations and *in situ* Raman spectroscopy, the interaction between SnO_2 and porous carbon fibers modulates the electron structure of Sn active centers with a stronger electron transfer to the carbon substrate. The alteration in electron state density precipitates a shift in the *d*-band center, thereby promoting the adsorption of pivotal intermediates involved in formate formation. In addition, the porous structure is beneficial to improve the exposure and utilization rate of the active sites. The mass activity can reach up to 7.09 A/mg on SnO_2PCNF, which is 124 times higher than that of support-free SnO_2 nanoparticles (0.057 A/mg). This research offers valuable insights for the development of freestanding electrodes with high electrocatalytic activity and metallic utilization.

Declaration of competing interest

The authors declare that they have no known competing financial interests or personal relationships that could have appeared to influence the work reported in this paper.

Acknowledgments

This work was supported by the National Natural Science Foundation of China (Nos. 22172099, U21A20312), Guangdong Basic and Applied Basic Research Foundation (Nos. 2023A1515012776, 2022B1515120084), and the Shenzhen Science and Technology Program (No. RCYX20200714114535052). We also acknowledge the Instrumental Analysis Centre of Shenzhen University for performing TEM.

Supplementary materials

Supplementary material associated with this article can be found, in the online version, at doi:10.1016/j.cclet.2024.109555.

References

[1] S. Perathoner, G. Centi, ChemSusChem 7 (2014) 1274–1282.
[2] D. McCollum, N. Bauer, K. Calvin, A. Kitous, K. Riahi, Climatic Change 123 (2014) 413–426.

[3] E.V. Kondratenko, G. Mul, J. Baltrusaitis, G.O. Larrazábal, J. Pérez-Ramírez, Energy Environ. Sci. 6 (2013) 3112–3135.
[4] R.S. Haszeldine, Science 325 (2009) 1647–1652.
[5] M. Gong, C. Cao, Q.L. Zhu, EnergyChem 5 (2023) 100111.
[6] S. Garg, M. Li, A.Z. Weber, et al., J. Mater. Chem. A 8 (2020) 1511–1544.
[7] S.A. Al-Tamreh, M.H. Ibrahim, M.H. El-Naas, et al., ChemElectroChem 8 (2021) 3207–3220.
[8] Y. Wang, D. Wang, Y. Li, Adv. Mater. 33 (2021) 2008151.
[9] C. Tang, Y. Zheng, M. Jaroniec, S.Z. Qiao, Angew. Chem. Int. Ed. 60 (2021) 2–21.
[10] D.D. Ma, S.G. Han, S.H. Zhou, et al., CCS Chem. 5 (2023) 1827–1840.
[11] G. Chen, D. Ye, R. Chen, et al., J. CO2 Util. 44 (2021) 101409.
[12] S. Zhao, S. Li, T. Guo, et al., Nano-Micro Lett. 11 (2019) 1–19.
[13] F. Cheng, X. Zhang, K. Mu, et al., Energy Technol. 9 (2021) 2000799.
[14] T.D. Nguyen-Phan, J.E. Ellis, A.V. Nagarajan, et al., Appl. Catal. B: Environ. 340 (2024) 123250.
[15] Y. Pei, W. Gu, S. Cheng, et al., ACS Catal. 13 (2023) 12082–12091.
[16] H. Wang, N. Wen, Y. Wang, et al., Adv. Funct. Mater. 32 (2023) 2303473.
[17] Q. Zhang, M. Sun, C.Y. Yuan, et al., ACS Catal. 13 (2023) 7055–7066.
[18] P.F. Yin, J. Fu, Q. Yun, et al., Adv. Mater. 34 (2022) 2201114.
[19] M. Chu, C. Chen, Y. Wu, et al., Green Energy Environ. 7 (2022) 792–798.
[20] J.H. Kim, H. Woo, J. Choi, H.W. Jung, Y.T. Kim, ACS Catal. 7 (2017) 2101–2106.
[21] T.W. van Deelen, C. Hernández Mejía, K.P. de Jong, Nat. Catal. 2 (2019) 955–970.
[22] Y. Pi, Z. Qiu, Y. Sun, et al., Adv. Sci. 10 (2023) 2206096.
[23] Y. Lou, J. Xu, Y. Zhang, et al., Mater. Today Nano 12 (2020) 100093.
[24] G. Liu, Q.T. Trinh, H. Wang, et al., Small 19 (2023) 2301379.
[25] X. Wang, T. Bürgi, Angew. Chem. Int. Ed. 62 (2023) e202300146.
[26] Y. Li, T. Xu, Q. Huang, et al., ACS Catal. 13 (2023) 7597–7605.
[27] Z. Gao, J. Li, Z. Zhang, W. Hu, Chin. Chem. Lett. 33 (2022) 2270–2280.
[28] C. Liu, Q. Li, W. Kang, et al., J. Mater. Chem. A 10 (2022) 10–49.
[29] M. Wang, J. Yang, X. You, et al., Int. J. Hydrogen Energy 47 (2021) 2114–2123.
[30] H. Yang, X. Wang, Q. Hu, et al., Small Methods 4 (2020) 1900826.
[31] Q. Wang, F. Liu, Z. Jin, et al., Adv. Funct. Mater. 30 (2020) 2002580.
[32] Y. Zhang, X. Xia, X. Cao, et al., Adv. Energy Mater. 7 (2017) 1700220.
[33] S. Ding, Q. Chen, S. Chen, Y. Tian, J. Zhang, Chin. Chem. Lett. 34 (2023) 108232.
[34] H. Chen, L. Ding, W. Sun, et al., RSC Adv. 5 (2015) 56401–56409.
[35] X. Jiang, X. Li, Y. Kong, et al., Small 18 (2022) 2204148.
[36] J. Yang, R. Hübner, J. Zhang, et al., Angew. Chem. Int. Ed. 60 (2021) 9590–9597.
[37] G. Jia, Y. Wang, M. Sun, et al., J. Am. Chem. Soc. 145 (2023) 14133–14142.
[38] M. Sharma, R.N. Aljawfi, K. Kumari, et al., J. Mater. Sci. Mater. Electron. 30 (2019) 760–770.
[39] Y. Zhao, X.G. Zhang, N. Bodappa, et al., Energy Environ. Sci. 15 (2022) 3968–3977.
[40] X. Lu, C. Zhu, Z. Wu, et al., J. Am. Chem. Soc. 142 (2020) 15438–15444.
[41] A. Heyns, J. Chem. Phys. 84 (1986) 3610–3616.
[42] I.V. Chernyshova, P. Somasundaran, S. Ponnurangam, Proc. Natl. Acad. Sci. U. S. A. 115 (2018) E9261–E9270.
[43] Z. Li, B. Sun, D. Xiao, et al., Angew. Chem. Int. Ed. 62 (2023) e202217569.